# Three-Dimensional Unsteady Analysis of Fluid–Structure Interaction in Check Valves of Diaphragm Volumetric Pumps

Ali Shakir Hial Alaqra

## Abstract

A comprehensive unsteady three-dimensional numerical model employing dynamic meshing techniques has been (FSI) occurring within the non-return. This advanced 3D CFD model offers a more precise representation of flow dynamics and a more accurate assessment of valve motion behavior compared to the earlier 2D model previously introduced by the authors. The improved model particularly enhances the understanding of internal volumetric losses caused by valve movement, which negatively impact the overall efficiency of the pump. The study investigated both piston-type and deformable diaphragm geometries under sinusoidal displacement conditions. Results showed comparable performance in terms of basic pump functionality for both configurations. Detailed simulations under normal operating and free-discharge conditions revealed increased instability in the check valves when the supplied air pressure was low .Notably, the exhaust valve exhibited significant valve "tapping," characterized by repeated strong fluid–structure interactions. In contrast, the intake (aspirating) valve demonstrated more stable sealing behavior, with only minor reopening observed at the onset of the backward stroke. These numerical insights have proven valuable for pump manufacturers, informing improvements in valve design, material selection, and maintenance strategies. The findings have directly contributed to the development of new and more efficient pump prototypes.

**Keywords:** 3D CFD، Fluid, Structure Interaction، Check Valves، Pumps

# تحليل ثلاثي الأبعاد غير مستقر لتفاعل السوائل مع البنية في صمامات عدم الرجوع للمضخات الحجمية الغشائية

علي شاكر حيال الأقرع

**الملخص:**

تم تطوير نموذج عددي شامل ثلاثي الأبعاد وغير مستقر يعتمد على تقنيات الشبكات الديناميكية ( Dynamic Meshing) لدراسة ظاهرة التفاعل بين المائع والبنية الصلبة (Fluid–Structure Interaction - FSI) داخل صمام عدم الرجوع (Non-return Valve). يوفّر هذا النموذج العددي المتقدّم في ميكانيكا الموائع الحسابية (D CFD3) تمثيلاً أكثر دقة لديناميكية الجريان، وتقييماً أكثر واقعية لسلوك حركة الصمام، مقارنةً بالنموذج ثنائي الأبعاد (D2) الذي قدّمه الباحثون في دراسة سابقة. يسهم هذا النموذج المحسَّن بشكل خاص في توضيح الفواقد الحجمية الداخلية الناتجة عن حركة الصمام، والتي تؤثر سلبًا في الكفاءة الكلية للمضخة. تضمّنت الدراسة تحليل كل من هندسة المكبس (Piston-type) وغشاء التحميل المرن ( Deformable Diaphragm) تحت ظروف إزاحة جيبية (Sinusoidal Displacement). وقد أظهرت النتائج أن أداء كلا التكوينين متقارب من حيث الوظائف الأساسية للمضخة. كما كشفت المحاكاة التفصيلية، في ظروف

التشغيل الاعتيادية وأثناء التصريف الحر، عن ازديادٍ في عدم استقرار صمامات الفحص ( Check Valves) عند انخفاض ضغط الهواء المزوّد. ومن الملاحظ أن صمام العادم أظهر ظاهرة «الارتطام المتكرر للصمام» (Valve Tapping)، الناتجة عن التفاعلات القوية والمتكررة بين المائع والبنية الصلبة، في حين أظهر صمام السحب (Intake Valve) سلوك إغلاق أكثر استقرارًا، مع إعادة فتح طفيفة فقط عند بداية شوط الرجوع الخلفي. قدّمت هذه النتائج العددية رؤى تطبيقية مهمة لمصنّعي المضخات، إذ أسهمت في تحسين تصميم الصمامات، واختيار المواد المناسبة، ووضع استراتيجيات صيانة أكثر كفاءة. كما ساعدت النتائج مباشرةً في تطوير نماذج أولية جديدة لمضخات ذات كفاءة أعلى.

**الكلمات المفتاحية**: النمذجة العددية ثلاثية الأبعاد (D CFD3)؛ التفاعل بين المائع والبنية الصلبة (FSI)؛ صمامات الفحص (Check Valves)؛ المضخات.

## 1. Introduction

Air-Operated Diaphragm Pumps: Design Evolution and Performance Analysis A diaphragm pump belongs to the category of positive displacement machines and operates by flexing a resilient membrane to displace fluids. It is especially suitable for handling viscous or abrasive liquids. The pumping mechanism relies on a set of one-way (check) valves to prevent reverse flow during the reciprocating motion[1].Among the various configurations, Air-Operated Double Diaphragm (AODD) pumps are widely used. These systems feature two diaphragms driven alternately by compressed air via a shuttle valve system, with four check valves guiding the flow. The diaphragm not only facilitates fluid movement but also acts as a dynamic sealing component, eliminating the need for traditional seals, lubrication, and minimizing internal leakage or mechanical wear Despite their simplicity and robustness, AODD pumps face common issues related to check valve wear over time—such as deformed valve seats, worn balls, misaligned guides, and damaged O-rings—primarily caused by cyclic mechanical stress and fatigue[2].From Empirical Design to Simulation-Based Development Historically, diaphragm pump development has heavily relied on empirical testing to assess material behavior, flow characteristics, and component durability under varied conditions. While industry standards offer guidance, design enhancements have often stemmed from iterative, trial-based processes—frequently inspired by existing commercial designs and limited to proven, incremental changes.With the growing demand for faster and more economical prototyping, advanced simulation technologies, particularly Computational Fluid Dynamics (CFD), have become indispensable in modern pump engineering. In response, SAMOA Industrial S.A., a leading European manufacturer of fluid handling solutions, has developed a next-generation AODD pump lineup with an overhauled internal flow architecture—optimized using CFD simulations during early design stages[3]. Innovative CFD Methodology for Diaphragm Pump Simulation In previous research conducted by the authors, a novel CFD approach was introduced for analyzing diaphragm pump performance. This method used a deformable mesh to accurately model the diaphragm's transient deformation and the fluid–structure interaction (FSI) with the check valve balls. Comparable numerical strategies have been employed in the study of other positive displacement pumps, such as axial piston, plunger, vane, and air-operated piston pumps.Subsequent research has also examined suction dynamics, geometric optimization, and flow behavior involving non-Newtonian fluids. More recently, CFD studies have incorporated cavitation models to better capture suction-related effects, with increasing emphasis on simulating the dynamic interaction between valve elements and diaphragm/piston motion[4]. Early FSI simulations used deforming grids to represent the ball motion in high-pressure safety valves, disk valves, and other reciprocating systems. More complex studies now analyze discharge valve behavior within full 3D pump geometries, such as plunger and reciprocating piston pumps[4]. Parallel advancements have been made in modeling both linear and rotary compressors using commercial CFD tools like ANSYS Fluent® and ADINA®. However, comprehensive CFD research on diaphragm pumps remains scarce. Notable exceptions include studies on piston-diaphragm pumps with spring-loaded check valves using immersed boundary methods and simplified FSI models. These spring-based models help improve numerical convergence by limiting valve displacement. In contrast, systems without springs require explicit modeling of mechanical stops, as demonstrated in [5], with strict control over time-step resolution to ensure numerical accuracy.

Extending from 2D to Full 3D Pump Simulation

The earlier 2D simulations achieved strong agreement with experimental data, particularly in capturing flow behavior around the check valves. Building on this, the current study presents a comprehensive 3D simulation using an implicit solver for both mesh movement and governing fluid equations. The Unsteady Reynolds-Averaged Navier–Stokes (URANS) method is applied, along with the RNG k–ε turbulence model[6].

Initially, the diaphragm motion is approximated using a cylindrical piston that generates an equivalent stroke volume. The mesh is refined near valve seats to resolve the complex FSI between the fluid and valve balls at different phases of the pumping cycle. Both the 2D and full 3D results are compared under varying operating pressures to assess overall pump behavior and localized valve dynamics—especially oscillatory motions and impacts during valve operation The enhanced model eventually incorporates the actual 3D geometry of the flexible diaphragm, yielding similar overall performance to the simplified piston model, but revealing richer internal dynamics—such as significant flow recirculation, swirl effects in the discharge manifold, and valve ball oscillations with associated leakage and time delays during opening/closing cycles[7].

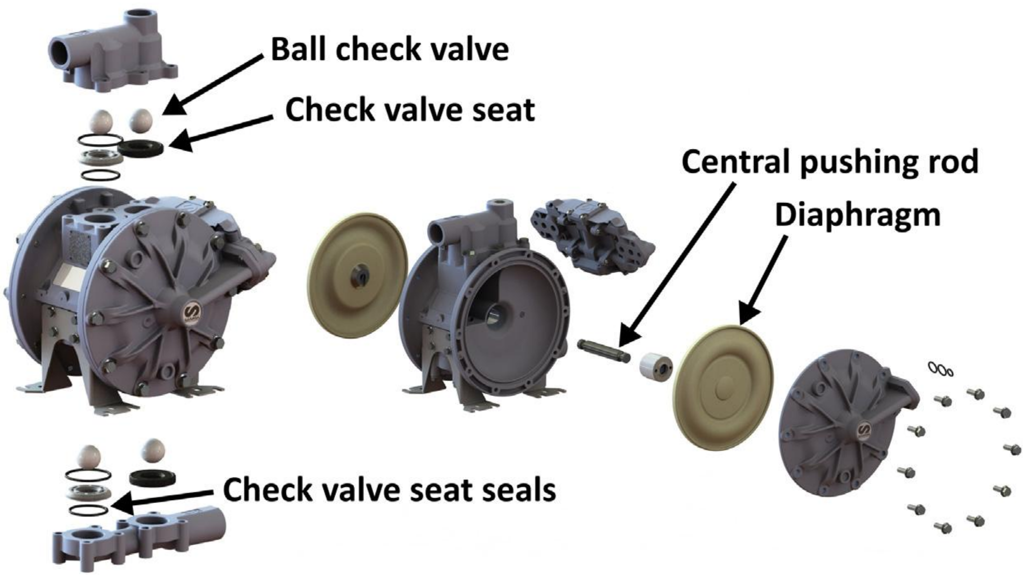


Fig. 1. DP-200 pump: 3D view of the operative components[7]

Table 1. Geometrical data and operating parameters[7]

| | |
|---|---|
| Diaphragm external diameter, $D_e$ (mm) | 200 |
| Diaphragm internal diameter, $D_i$ (mm) | 100 |
| Diaphragm effective diameter, $D_d$ (mm) | 150 |
| Diaphragm stroke length, $L_d$ (mm) | 31.0 |
| Diaphragm effective area, $A_d$ ($cm^2$) | 176.7 |
| Delivery per stroke, $V_d$ ($cm^3$) | 548 |
| Internal manifolds diameter, $D_m$ (mm) | 26.5 |
| Ball diameter of check valves, $D_v$ (mm) | 31.75 |
| Ball maximum displacement, $L_v$ (mm) | 10 |
| Check valve effective area (max), $A_v$ ($cm^2$) | 4.98 |
| Air-operation pressure, $P_{air}$ (bar) | 0–8 |
| Pressure ratio (−) | 1:1 |
| Maximum free delivery (8 bar), Q (l/min) | 200 |
| Maximum driven velocity, n (Hz) | 3.0 |

Print ISSN 2710-0952 Electronic ISSN 2790-1254

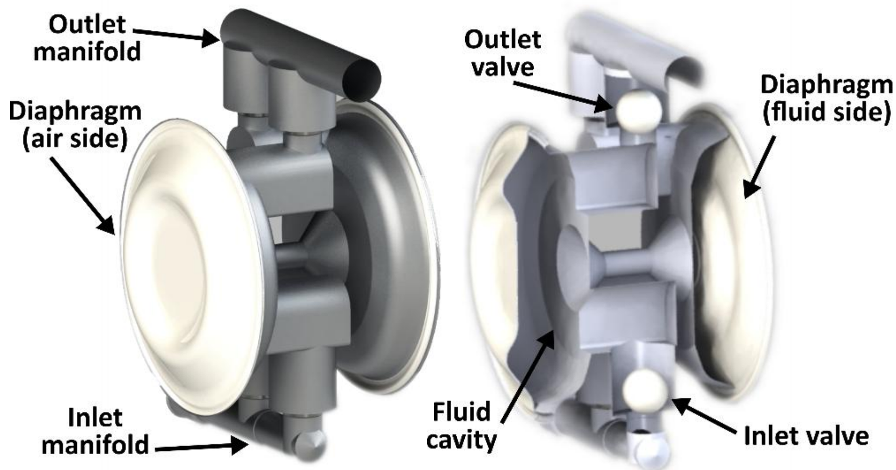


Figure 2. DP-200 pump: Rendered view of cavities and flow passages[8].

## Numerical Modeling and Experimental Characterization

For the purposes of this study, a three-dimensional digital model was developed to represent the internal flow paths and chambers of the AODD pump, as depicted in Figure 2. The illustration on the left-hand side outlines the essential components necessary to replicate the pump's operational behavior, while the right-hand diagram defines the computational domain used for numerical discretization[9].

To enhance computational efficiency without sacrificing modeling fidelity, the simulation leveraged the pump's inherent geometric symmetry. As a result, only one half of the pump assembly—including a single diaphragm and its associated pair of check valves—was modeled.

To conclude this section, the pump's performance characteristics—sourced from the manufacturer's technical datasheet—are displayed in Figure 3. Experimental testing was carried out under air supply pressures of 2, 4, and 6 bar. A range of outlet pressures was achieved by adjusting a throttle valve positioned within the discharge manifold Pressure measurements were taken using two TE Connectivity MEAS U5244 pressure transducers, each rated for a measurement range of -1 to 13 bar with a stated accuracy of ±1%. Volumetric flow rates were determined using an electronic balance, enabling a mass-based calculation of throughput. The maximum estimated uncertainties were ±0.12 bar in pressure and ±0.7% in flow rate.

Experimental results are plotted as black data points in Figure 3 and are accompanied by linear trendlines (solid black lines, referenced to the left y-axis) for clarity. In addition, air consumption was monitored using a Testo 6442 thermal mass flowmeter, which offers a wide measurement range (12 to 3750 liters per minute) and a measurement accuracy of ±0.3%.

To provide deeper insight into performance, efficiency isolines (thin grey lines) are overlaid on the graph, delineating regions of constant pump efficiency under varying operating conditions.Finally, the hydraulic chamber pressure was continuously monitored using an ESI Genspec GS4002 sensor. This transducer was chosen for its broad operational range (-1 to 24 bar), ensuring protection against potential damage from transient pressure spikes. Like the other sensors, it maintains a ±1% accuracy, delivering reliable measurements even under dynamically fluctuating pressures[10]

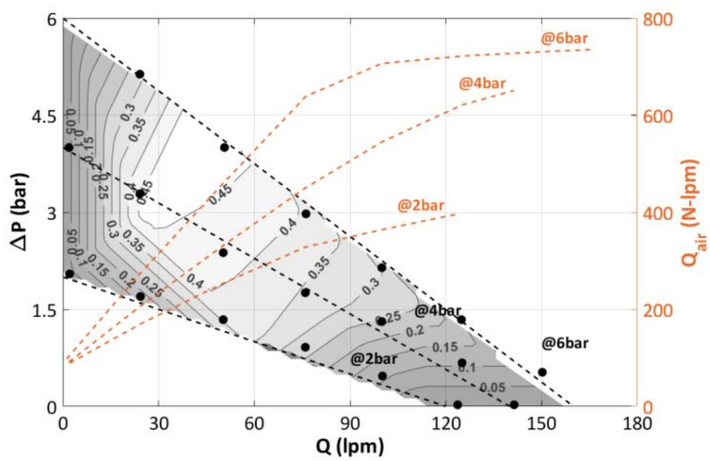


.

Figure 3. DP-200 Pump: Experimental performance curves at varying air-supply pressures.

## 3. Three-Dimensional Numerical Model

The computational analyses conducted in this study utilized ANSYS Fluent® v16.2 [27], a commercial CFD platform that numerically solves the using the Finite Volume Method (FVM). The three-dimensional model captures both the reciprocating motion of the diaphragm and the flow-induced dynamics of the check valve balls, which are resolved through Fluent's dynamic mesh functionality—implemented via a hybrid strategy combining local remeshing and layering algorithms[11].

To accurately resolve the fluid–structure interaction (FSI) phenomena inherent to the pump's operation, custom user-defined functions (UDFs) were developed and integrated into the solver environment. These UDFs embed a tailored implicit coupling algorithm [12], which enhances solution robustness and accelerates convergence by synchronizing mesh motion with fluid forces in a stable numerical framework.

### 3.1. Simplified 3D Geometry and Structured Meshing for Piston-Equivalent Diaphragm Motion

In the preliminary modeling phase, a simplified geometric approximation was adopted to reduce computational overhead. Specifically, the deformable diaphragm was replaced by an idealized, rigid piston that reproduces the same volumetric stroke displacement. To ensure hydraulic equivalence, an effective diaphragm diameter was derived, maintaining mass conservation while allowing for a geometrically reduced and computationally efficient model.[13]

The computational domain was constructed using ANSYS ICEM CFD® v16.2 [14], employing a block-structured meshing strategy based on modular rectangular decomposition. This approach enabled the generation of a fully structured, body-fitted hexahedral mesh, offering enhanced control over grid resolution in critical regions—particularly around the valve seats, inlet/outlet manifolds, and narrow flow passages.Meshing methodology followed best practices established in the authors' previous 2D simulation work [15], including localized mesh refinement near solid boundaries and within small clearance regions around moving components. Special attention was paid to meshing the vicinity of the check valve balls, ensuring that dimensionless wall distances ($y^+$) were maintained within the optimal range of 4 to 9, thus supporting accurate turbulence modeling in the near-wall region throughout the pumping cycle.For the simplified piston-based diaphragm motion, a layering remeshing technique was employed to accommodate the linear stroke behavior. The mesh zone adjacent to the piston dynamically adapted during simulation—expanding during suction and collapsing during discharge. This was governed by Fluent's layering algorithm, with a split factor of 0.4 (triggering layer addition when cell height exceeded 140% of its original value) and a collapse factor of 0.2 (removing layers when compressed below 20% of initial height).[16]

The final mesh consisted of 111,575 structured hexahedral cells. Figure 4 illustrates the mesh topology in the diaphragm region and associated flow manifolds. A cross-sectional detail is provided to highlight the mesh refinement surrounding the check valve balls, demonstrating the high spatial resolution achieved in these dynamically sensitive zones

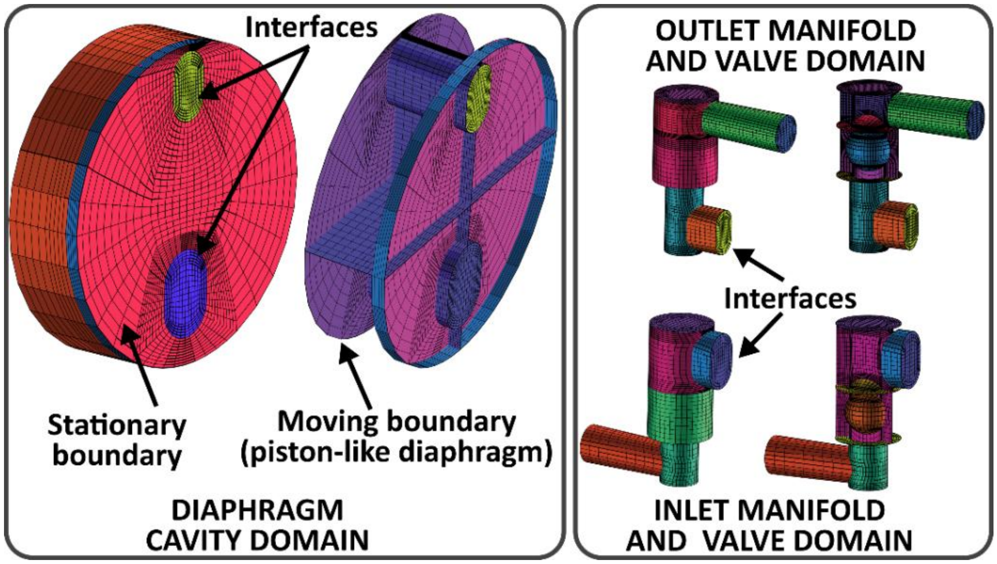


Figure 4. Mesh distribution in the piston-like diaphragm and the inlet/outlet manifolds featuring non-return valves[17].

**Complementary Mesh Configuration and Boundary Conditions**

To further support the mesh strategy outlined earlier, **Figure 5** offers a detailed visualization of the meshing approach employed in the numerical model. The **left panel** illustrates the **dynamic mesh zones**, where cells are either added or removed in real time as part of the **layering remeshing algorithm**. This mechanism accommodates the piston-like diaphragm's reciprocating motion by adjusting the local mesh structure accordingly. The **right panel** presents an overview of the **entire structured mesh** across the simulation domain, providing a global perspective on the discretization quality and topology.Additionally, the figure identifies the **primary boundary conditions** applied in the model:[18]

At the **inlet**, a **total pressure boundary condition** is imposed, set to **zero gauge pressure**, representing an open atmospheric suction condition.At the **outlet**, the boundary condition is defined via a **pressure loss model**, expressed as a function of the **local kinetic energy**. The pressure drop is modulated by a constant KvK_vKv, which emulates the **variable resistance introduced by a throttle valve**—thus allowing simulation of multiple operating scenarios by adjusting flow restriction.[19]

The motion of the **piston-equivalent diaphragm** is driven by a **compiled user-defined function (UDF)**, which imposes a **sinusoidal velocity profile** on the

Print ISSN 2710-0952 Electronic ISSN 2790-1254

diaphragm's center of gravity. This motion is described mathematically by the expression:[20]

This approach ensures a smooth and periodic displacement of the diaphragm surface, accurately replicating the pumping cycle within the simplified model.In parallel, the **fluid–structure interaction (FSI)** of the **check valve balls** is handled via a second **dedicated UDF**. This function calculates the **net hydrodynamic forces** acting on each ball at every time step and updates their positions accordingly. This dynamic response captures the transient interaction between the fluid flow and the mobile valve components, a critical factor in replicating real valve behavior.Further implementation details regarding these user-defined functions and the underlying FSI algorithms can be found in the authors' earlier work [21]

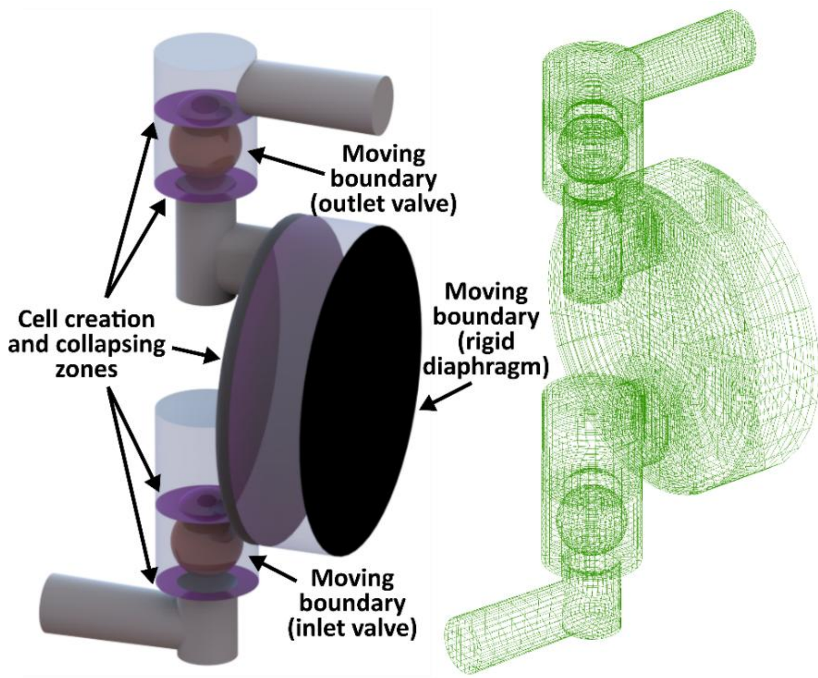


Figure 5. Mesh density in the piston-like membrane and inlet/outlet manifolds with adaptive layering mesh for the balls motion[21].

3.2. Solver and numerical model

In order employing deformable mesh functionalities. :[22]

المجلة العراقية للبحوث الإنسانية والإجتماعية والعلمية
Iraqi Journal of Humanitarian, Social and Scientific Research
Print ISSN 2710-0952 Electronic ISSN 2790-1254

- Continuity equation:

$$\frac{\partial \overline{u}_i}{\partial x_i} = 0 \qquad (1)$$

- Momentum equation:

$$\rho\frac{\partial \overline{u}_i}{\partial t} + \rho\frac{\partial(\overline{u_i}\overline{u_j})}{\partial x_j} = -\frac{\partial \overline{p}}{\partial x_i} + \mu\nabla^2\overline{u}_i + \frac{\partial \tau_{ij}}{\partial x_j} \qquad (2)$$

/here the Reynolds Stress Tensor in the momentum equation has been modelled using n Eddy Viscosity Model, according to:

$$\tau_{ij} = -\rho\overline{u_i' u_j'} = \mu_t \underbrace{\left(\frac{\partial \overline{u}_i}{\partial x_j} + \frac{\partial \overline{u}_j}{\partial x_i}\right)}_{S_{ij}} - \frac{2}{3}\rho k \delta_{ij} \qquad (3)$$

In the turbulence modeling framework, the turbulent kinetic energy is denoted by k, and the turbulent viscosity is represented accordingly, with a turbulence model constant Cμ=0.0845C_\mu = 0.0845Cμ=0.0845. For turbulence closure, the well-established two-equation RNG k-εk\text{-}\varepsilonk-ε model has been employed due to its recognized robustness and adaptability to a wide range of flow conditions. Preliminary sensitivity studies conducted with the Realizable k-εk\text{-}\varepsilonk-ε model yielded results that were nearly identical to those obtained with the RNG formulation—particularly in terms of valve dynamics and internal flow structures. In contrast, complementary tests using low-Reynolds-number k-ωk\text{-}\omegak-ω models showed excessive numerical damping, which suppressed important flow instabilities associated with the oscillation and tapping behavior of the check valve balls. As a result, the k-ωk\text{-}\omegak-ω family of models was deemed unsuitable for this specific application [5].
For the RNG k-εk\text{-}\varepsilonk-ε model used in this work, and neglecting any buoyancy effects, the closure equations take the following form

$$\rho\frac{\partial k}{\partial t} + \rho\frac{\partial(k\overline{u}_i)}{\partial x_i} = \frac{\partial}{\partial x_j}\left[\alpha_k\mu_t\frac{\partial k}{\partial x_j}\right] + 2\mu_t S_{ij}S_{ij} - \rho\varepsilon \qquad (4)$$

$$\rho\frac{\partial \varepsilon}{\partial t} + \rho\frac{\partial(\varepsilon\overline{u}_i)}{\partial x_i} = \frac{\partial}{\partial x_j}\left[\alpha_\varepsilon\mu_t\frac{\partial \varepsilon}{\partial x_j}\right] + C_{\varepsilon 1}\frac{\varepsilon}{k}(2\mu_t S_{ij}S_{ij}) - \rho C_{\varepsilon 2}\frac{\varepsilon^2}{k} \qquad (5)$$

Where the turbulent dissipation rate is defined as $\varepsilon = 2\nu\overline{s_{ij}' s_{ij}'}$, being $s_{ij}' = \frac{1}{2}\left(\frac{\partial u_i'}{\partial x_j} + \frac{\partial u_j'}{\partial x_i}\right)$; and typical coefficients $C_{\varepsilon 1} = 1.42$, $C_{\varepsilon 2} = 1.68$ and $\alpha_k = \alpha_\varepsilon \sim 1.383$ have been employed.

A second-order upwind scheme was selected for the discretization of the convective terms, ensuring a balance between numerical accuracy and stability. For the diffusive terms in the momentum equations, Green-Gauss cell-based gradient reconstruction was employed to calculate spatial gradients. rate (ε\varepsilonε) were also discretized using a second-order scheme to maintain consistency in numerical accuracy across the turbulence model.

A segregated solver was adopted, utilizing the PISO (Pressure-Implicit with Splitting of Operators) algorithm, which proved to offer a favorable trade-off between computational cost and numerical robustness. The convergence criteria were set to a residual of 10−610^{-6}10−6 for the continuity equation, and a minimum threshold of 10−510^{-5}10−5 for the implicit mesh motion solver. Both criteria were required to be satisfied before advancing to the next time step, ensuring high fidelity in both fluid flow and mesh deformation.

Time step sizes were carefully selected within the range of 5×10−55 \times 10^{-5}5×10−5 to 1×10−41 \times 10^{-4}1×10−4 seconds, optimizing the balance between computational stability and efficiency. These values were chosen to maintain a Courant number below unity throughout the domain, preventing the numerical wave propagation from outpacing the physical fluid motion, which is especially critical in narrow regions near the check valves undergoing significant mesh deformation.

Table 2 summarizes the main simulation parameters used across the computational database. Notably, smaller time steps were required in cases involving higher operating frequencies and supplied air pressures, due to increased fluid accelerations and valve dynamics. Furthermore, simulating a complete pump cycle typically required around 10,000 time steps per case.

In terms of computational resources, each full-cycle 3D simulation—based on a mesh containing approximately 111,575 cells—required approximately 450 CPU hours, equivalent to 3–4 weeks of wall-clock time, when run on a single workstation equipped with a 4-core Intel Core i7-5820K processor (3.3 GHz) and 64 GB of RAM

Table 2. Numerical database. Outlet BC and time step sizes.

| Test No. | Supplied pressure (bar) | Discharge pressure, $P_{RMS}$ (bar) | Loss coefficient, $K_v$ (-) | Driving frequency (Hz) | Time step, Δt (s) | N° time steps per cycle (-) |
|---|---|---|---|---|---|---|
| #1 | 2 | 0 | 0 | 1.85 | $1\cdot10^{-4}$ | 5,400 |
| #2 | 2 | 1.16 | 75.1 | 1.0 | $1\cdot10^{-4}$ | 10,000 |
| #3 | 4 | 0 | 0 | 2.45 | $1\cdot10^{-4}$ | 4,080 |
| #4 | 4 | 1.99 | 62.1 | 1.4 | $1\cdot10^{-4}$ | 7,140 |
| #5 | 4 | 3.65 | 1411 | 0.45 | $1\cdot10^{-4}$ | 22,220 |
| #6 | 6 | 0 | 0 | 2.7 | $5\cdot10^{-5}$ | 7,400 |
| #7 | 6 | 1.97 | 32.5 | 1.8 | $5\cdot10^{-5}$ | 11,110 |
| #8 | 6 | 3.63 | 139.9 | 1.25 | $1\cdot10^{-4}$ | 8,000 |
| #9 | 6 | 4.14 | 500.8 | 0.75 | $1\cdot10^{-4}$ | 13,330 |

3.3. Three-Dimensional Model with Deformable Diaphragm

Enhanced Modeling of Diaphragm Deformation

To improve the physical realism of the numerical simulations, an advanced modeling approach was introduced, extending the baseline model to incorporate the actual deformation behavior of the diaphragm in three dimensions. In this enhanced configuration, the previously idealized, rigid piston surface was replaced with a more representative diaphragm geometry, consisting of a rigid central circular disk bordered by a flexible annular membrane (see Figure 6).

The central plate is prescribed the same sinusoidal displacement used in the earlier simplified model, ensuring consistency in actuation dynamics. Meanwhile, the surrounding flexible annulus undergoes nonlinear deformation, adapting its shape radially to preserve geometric continuity and mechanical coherence throughout the diaphragm's oscillation.

Due to the geometric complexity introduced by the deformable annulus, the structured meshing strategy used previously was no longer suitable. The working fluid domain was therefore re-meshed using a fully unstructured tetrahedral grid, coupled with an automatic remeshing strategy. This technique employs a spring-based smoothing algorithm, which redistributes mesh nodes during minor boundary displacements. However, in regions of high deformation—especially near finely meshed areas—mesh quality can deteriorate due to excessive skewness or unfavorable aspect ratios, potentially compromising simulation stability.

To address this, any elements exceeding predefined mesh quality limits (such as skewness or cell size thresholds) were automatically flagged and subjected to localized remeshing. Solution variables from the original mesh were interpolated onto the new cells. This process utilized a spring factor of 0.9, with cell sizes constrained between 2 mm (minimum) and 10 mm (maximum), and a maximum

2025 تشر2ين 19A العـــدد المجلة العراقية للبحوث الإنسانية والإجتماعية والعلمية
No.19A Nov. 2025 Iraqi Journal of Humanitarian, Social and Scientific Research
Print ISSN 2710-0952 Electronic ISSN 2790-1254

allowable skewness of 0.7. The mesh update procedure was scheduled to run every 10 time steps to maintain consistent mesh quality throughout the simulation.

The resulting mesh for this deformable diaphragm model was a hybrid unstructured grid, comprising 101,957 elements. Although this mesh contained approximately 10% fewer cells than the piston-based model, the computational demand was significantly greater. Specifically, simulating a single full pumping cycle required approximately 550 CPU hours on the same workstation—an Intel Core i7-5820K (3.3 GHz, 4 cores, 64 GB RAM). After normalizing for cell count (via a 1.1 correction factor), the remeshing strategy was found to be approximately 30% slower than the layering method used in the simplified model.

Given the substantial increase in computational cost, the use of a fully deformable diaphragm is warranted only if significant discrepancies are observed between the results of the two modeling approaches. To evaluate this, a set of free-delivery operating conditions was selected for direct comparison. These conditions correspond to Test Cases #1, #3, and #6 as detailed in Table 5

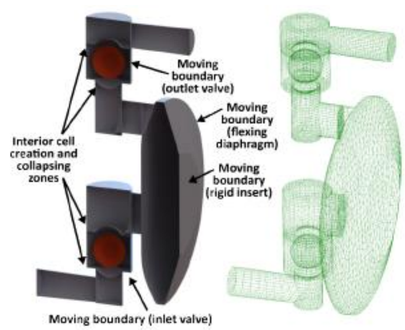


Figure 6. Mesh density in the deformable diaphragm and inlet/outlet manifolds with adaptive layering mesh.

## 4. Results and Discussion

### 4.1. Comparison of Performance Curves

The initial phase of the analysis focuses on validating the 3D numerical model by comparing the predicted flow rates with corresponding experimental measurements, as illustrated in Figure 7. The flow rate is plotted as a function of the discharge pressure to evaluate the pump's performance under varying load conditions. It is important to note that, due to the application of in the simulation—where only half of the pump geometry was modeled—the computed flow rates were doubled to provide a direct comparison with the full-pump experimental data.

The numerical predictions successfully reproduce the experimentally observed linear decrease in increases. At air supply pressures (2 and 4 bar), the model shows excellent agreement with experimental results, with maximum relative errors limited to approximately 6%, as summarized in Table 3.

For the higher air supply pressure of 6 bar, while the overall trend of flow reduction with increasing discharge pressure remains adequately captured, the numerical model exhibits larger deviations. Here, the maximum relative error reaches nearly 19%. These discrepancies are largely attributed to the increased influence of elevated air pressure on the stroke stability, which notably affects the diaphragm motion and check valves. This complex interplay induces phenomena such as valve instabilities and valve ball tapping, which contribute to the observed divergence and will be examined in greater detail in the subsequent section

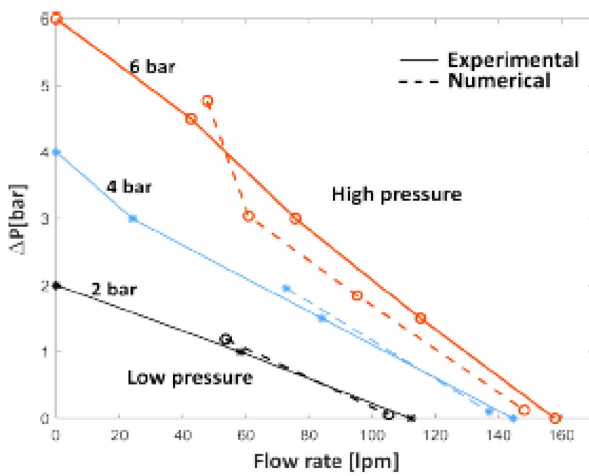


Figure 7. Comparison of experimental and numerical performance curves.

4.2. Pressure Evolution in the Working Chamber

The transient pressure fluctuations within the diaphragm's working chamber are presented operating scenarios in **Figure 8**, comparing numerical predictions against corresponding experimental data. For additional context, previously published results from a **2D numerical model** are also shown to facilitate a comparative evaluation.

The **left panel** displays the pressure variation under conditions of **high air supply pressure (6 bar)** paired with a at the outlet. In contrast, the **right panel** illustrates the pressure response under **low air supply pressure (2 bar)** combined with a **similarly low exhausting pressure (1 bar)**.

It should be noted that the experimental pressure measurements were derived through an **ensemble averaging process** over more than 20 operating cycles. This

Print ISSN 2710-0952 Electronic ISSN 2790-1254

averaging significantly reduces measurement noise and improves the reliability of the data for meaningful comparison with the numerical results

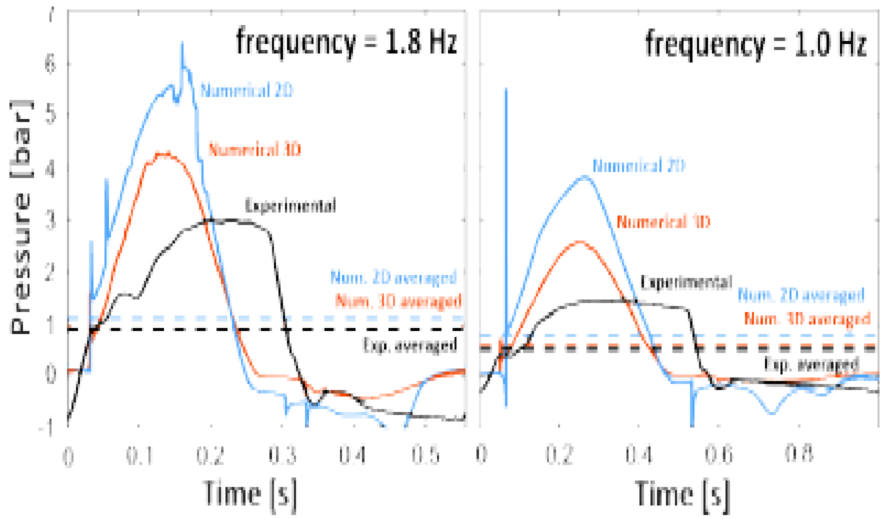


**Figure 8.** Comparison of experimental and numerical pressure evolutions within the working cavity at high (left) and low (right) air supply pressures under standard operating conditions.

The 3D numerical model demonstrates significantly improved accuracy in capturing inside the diaphragm cavity compared to the 2D simulations. Under (left panel), the experimental pressure profile exhibits a pronounced sinusoidal shape, indicating a strong bidirectional coupling between the air supply pressure and the diaphragm dynamics. This interaction likely contributes to the larger discrepancies observed in the pump performance curves. While the numerical pressure closely follows the sinusoidal pattern imposed by the prescribed piston motion, the 2D model shows greater instability and reduced precision. Notably, the root mean square (RMS) values of the pressure fluctuations—indicated by dashed mean lines—align closely between the experimental data and the 3D simulation, whereas the 2D model tends to overestimate these fluctuations.

In contrast, under low air supply pressure conditions (right panel), the experimental pressure profile reveals a stepped waveform rather than a smooth sinusoid. This suggests a diminished influence of hydraulic conditions on the instantaneous air supply pressure, supporting the assumption of sinusoidal diaphragm motion used in both 2D and 3D models. Here again, strong agreement exists between the time-averaged pressures from experimental measurements and the 3D simulation, while the 2D model consistently overpredicts the mean pressure and exhibits exaggerated pressure peaks during valve opening and closing events.

Print ISSN 2710-0952 Electronic ISSN 2790-1254

Subsequent sections will delve deeper into the internal flow structures and the dynamic responses of pump components under both high (6 bar, ~1.8 Hz) and low (2 bar, ~1.0 Hz) air supply pressures. These analyses cover operating outlet pressures ranging from 1.0 to 1.5 bar, reflecting typical industrial conditions, as well as free-delivery scenarios.

### 4.3. Standard Operation: Comparison of 2D and 3D Results

generally function within an outlet pressure range of 1.0 to 1.5 bar, despite known efficiency trade-offs. This range is often described as "standard operation" by manufacturers and is prevalent across many industrial diaphragm pump applications. The following discussion examines the internal pump behavior at both high and low delivered flow rates within this operating window.

#### 4.3.1. Delivered Flow Rate and Response of Non-Return Valves

Figure 9 compares the evolution of flow rate, cavity pressure, and the unsteady behavior of at a high driving frequency, as predicted by 2D and 3D models. The 2D results (left subplots) reveal sharp pressure spikes inside the cavity, only partially damped in (blue line in the third subplot) displays instability during the suction phase, characterized by an indistinct closure that does not substantially affect the inflow rate.

In contrast, the 3D results (right subplots) exhibit more consistent and physically realistic flow dynamics. The discharge valve flow rates are slightly lower than theoretical expectations.

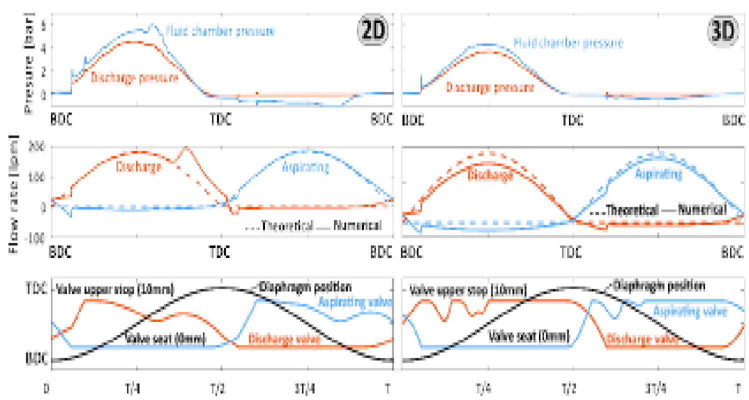


Figure 9. Temporal changes in the diaphragm cycle's pressure, flow rate, and check valve response are compared between 2D (left) and 3D (right) findings when the air supply pressure is high.

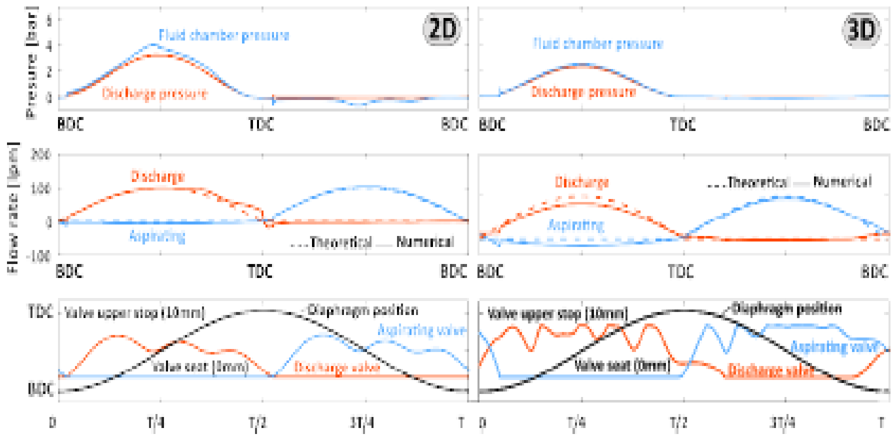


**Figure 10.** Comparison of the temporal evolution of pressure, flow rate, and check valve responses during the diaphragm cycle between 2D (left) and 3D (right) simulations under low air-supplied pressure conditions.

### 4.3.2. Comparison of 2D and 3D Simulations of the Development of the Opening in the Non-Return Valves

A detailed analysis of the oscillatory behavior of the check valves during standard operation at high driving frequencies is presented in Figures 11 and 12, focusing respectively on the discharge and aspirating valves. These figures provide instantaneous flow field contours illustrating velocity magnitude around the valve balls, offering enhanced physical insight into the partial valve closures. In addition, the temporal evolution of the forces acting on the balls is shown to clarify the observed dynamic fluctuations.

For the discharge valve (Figure 11), the 2D simulations predict a single oscillation near the end of the discharge hemicycle, which corresponds to an abrupt increase in the force exerted on the ball. Initially, the diaphragm stroke displaces the ball fully (first snapshot), after which the ball begins moving downward. At this stage, two high-velocity jets form around the ball (second snapshot), inducing a local pressure drop that generates significant suction, tending to re-open the valve gap (third snapshot). Finally, as the forward stroke concludes, the ball returns to its seat (fourth snapshot). It is important to note that the formation of these high-velocity jets around the 2D circular representation of the ball is not physically realistic and arises primarily due to geometric limitations of the two-dimensional domain.

In contrast, the 3D simulations (depicted via a transverse section in Figure 11) reveal a nearly instantaneous valve opening (first snapshot), followed by a rapid partial closure (second snapshot). This closure is quickly counteracted by the development of a high-velocity region near the ball (third snapshot) as the forward stroke approaches its maximum acceleration at T/4T/4T/4. Subsequently, a second rebound stabilizes, reinforced by the incoming fluid propelled by the diaphragm motion. This jet-induced suction maintains the valve in an open state and sustains a high force on the ball (fourth snapshot) throughout the latter half of the hemicycle

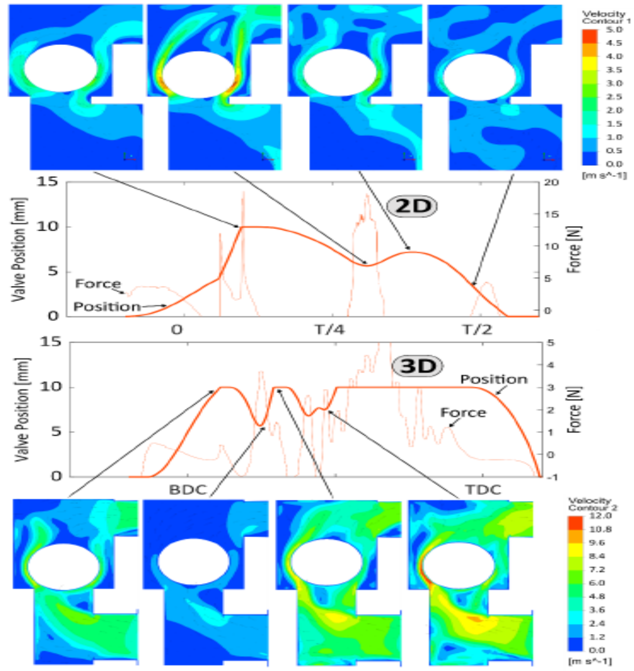


Figure 11. Response of the discharging non-return valve over the operative cycle for high air-supplied pressure. Comparison of 2D (top) and 3D (bottom) computations.

Figure 12 provides similar conclusions with respect the aspirating valve. In this case, the ball dynamics and the surrounding flow patterns are induced by the under pressure associated to the backward stroke. Consequently, the flow patterns are more uniform and high velocity jets are less pronounced with more evenly distributions around the check valve.

المجلة العراقية للبحوث الإنسانية والإجتماعية والعلمية
Iraqi Journal of Humanitarian, Social and Scientific Research
Print ISSN 2710-0952 Electronic ISSN 2790-1254

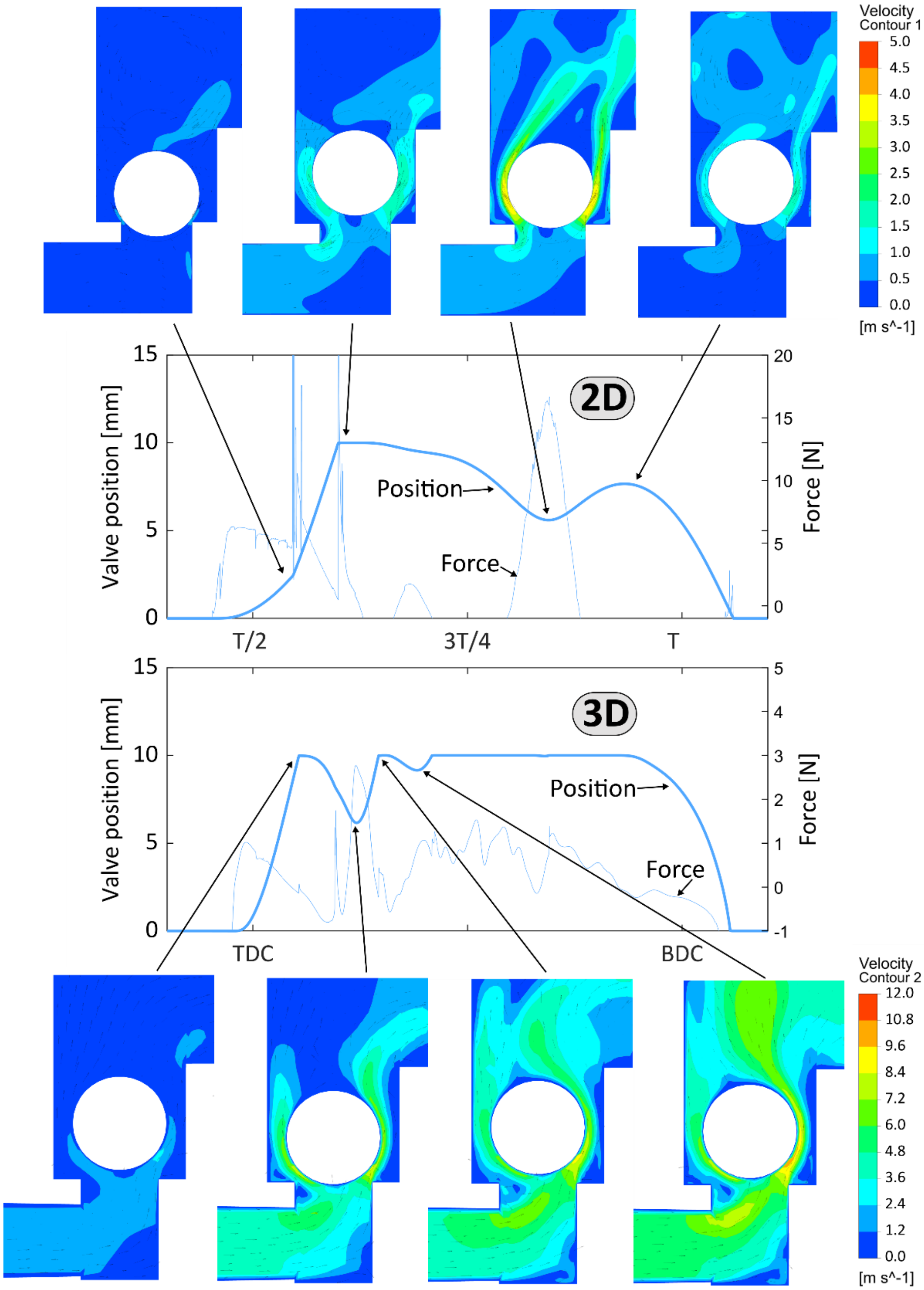


Figure 12. Response of the aspirating non-return valve over the operative cycle for low air-supplied pressure. Comparison of 2D (top) and 3D (bottom) computations.

Print ISSN 2710-0952 Electronic ISSN 2790-1254

4.3.3. Evolution of Flow Patterns within the Pump Internal Cavities: Comparison of 2D and 3D Maps

The comparison between the 2D and 3D models concludes with an analysis of the internal flow patterns inside the pump under high air-supplied pressure conditions (6 bar) during standard operation, as illustrated in Figures 13 and 14, respectively.

Figure 13 presents the 2D flow patterns through contours of velocity magnitude at four key intermediate positions throughout the operating cycle. Notably, the exhaust valve is only partially open at t=T/4t = T/4t=T/4, remaining nearly closed at the other sampled times. Several fluid recirculation zones appear within the internal passages, with the final snapshot at the bottom dead center (BDC) of the diaphragm stroke (t=Tt = Tt=T) revealing up to five distinct recirculating cells. Additionally, flow separation is evident in the outlet manifold at t=T/4t = T/4t=T/4, while the suction flow is clearly and accurately guided as it enters the working chamber of the diaphragm at t=3T/4t = 3T/4t=3T/4.

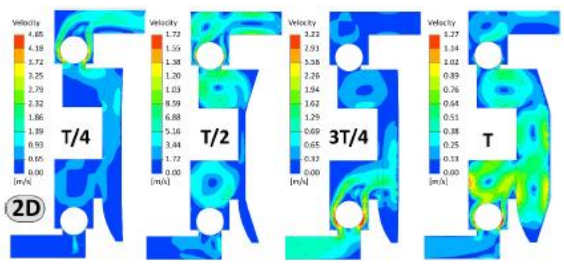


Figure 13. 2D description of flow patterns for high air-supplied pressure.

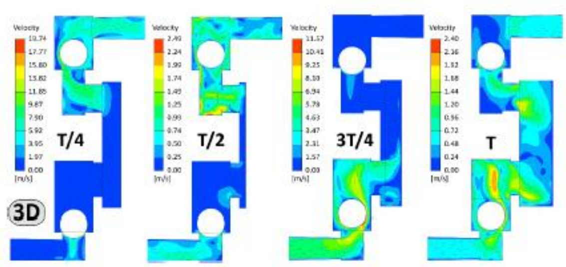


Figure 14. 3D description of flow patterns for high air-supplied pressure.

4.4. Free-Delivery Conditions

Print ISSN 2710-0952 Electronic ISSN 2790-1254

Diaphragm pumps are typically operated under free-delivery conditions when maximum output flow rates are required, such as during tank draining. In these scenarios, the pump is more prone to internal instabilities and oscillations, which lead to ball valve tapping and increased vibration, particularly at higher operating frequencies—up to 2.8 Hz in this study. The numerical results discussed here are exclusively derived from the 3D model simulations.

4.4.1. Evolution of Discharged Flow Rate and Pressure as a Function of the Non-Return Valves' Response

Figure 15 illustrates the temporal evolution of the pressure within the working chamber alongside the delivered flow rate under high air-supplied pressure (left plots). Since the discharge pressure is atmospheric, the pressure inside the diaphragm cavity primarily reflects the pressure losses occurring within the internal pump circuit. Notably, pressure peaks during free-delivery are more pronounced compared to those observed under standard operating conditions. Moreover, during the aspiration phase of the working chamber (indicated by the blue line in the top-left plot), significant under-pressures approach -1 bar, which heightens the risk of cavitation inception. Volumetric losses are also elevated relative to standard operation.

The right plots in Figure 15 depict the dynamic response of the valve balls, showing their positions (solid thick lines), velocities (solid thin lines), and the hydrodynamic forces acting upon them (dashed lines). The valve balls experience oscillations with maximum velocities around 1 m/s and peak hydrodynamic forces reaching approximately 100 N, predominantly during the closure of the aspirating valve. Furthermore, the data indicate a delay of about one-eighth of the cycle period before the balls fully close, confirming that valve closure is not instantaneous

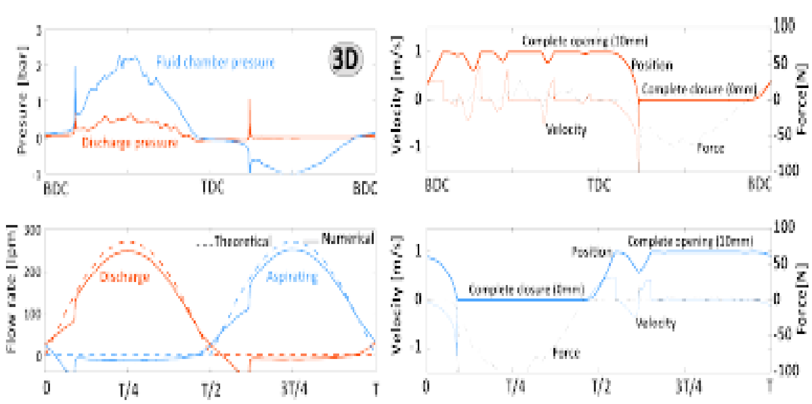

Print ISSN 2710-0952   Electronic ISSN 2790-1254

Figure 15. Temporal evolution of pressure and flow rate (left) and response of the no return valves (right) in the case of free delivery for high air-supplied pressure.

.

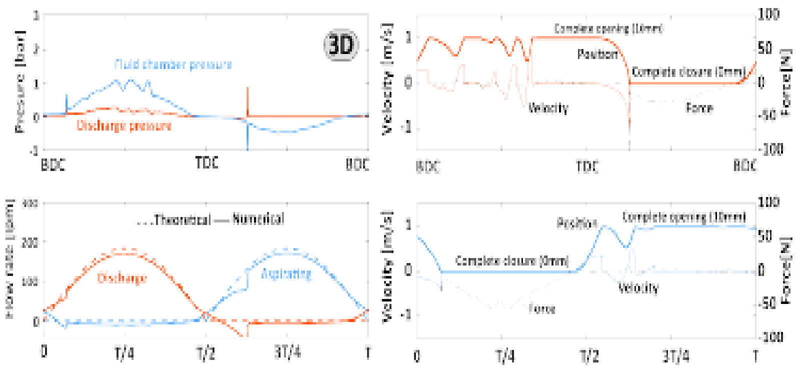


Figure 16. Temporal evolution of pressure and flow rate (left) and response of the nonreturn valves (right) in the case of free delivery for low air-supplied pressure.

4.4.2. Changes in the flow patterns within the cavities during free delivery.

The working chamber's velocity map evolution (3D results only) is depicted in Figure 17, which may be compared to earlier findings in Figure 14 for normal operation. Though greater gradients are found in the case of the free delivery condition, overall patterns are similar. At t=T/4, the velocity gradients are noticeably higher, especially close to the discharge valve. Additionally, because the piston is driving at a greater frequency at t=3T/4, the valve side near the diaphragm shows higher velocities.

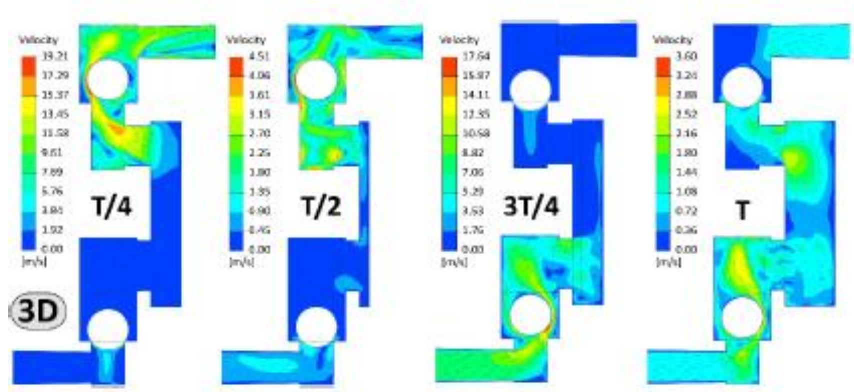


Figure 17. 3D description of flow patterns under free-delivery conditions.

leakages at the ball seats, caused by the partial re-opening of the valves

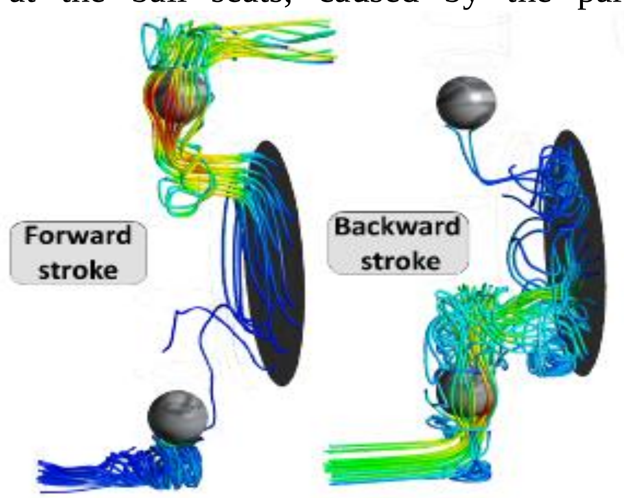


Figure 18. Streamlines in the internal cavities of the pump. Comparison of forward (left) and backward (right) strokes at free-delivery conditions.

4.5. Deformable (Real) Diaphragm vs. Piston-like (Approach) Diaphragm

. This effect influences the discharge non-return valve dynamics, resulting in only two valve re-openings instead of multiple oscillations. In contrast, the aspirating valve's response remains largely unchanged between models. Importantly, the deformable diaphragm model demonstrates a marked improvement in volumetric efficiency

تشر2ين 2025 العـــدد 19A المجلة العراقية للبحوث الإنسانية والإجتماعية والعلمية
No.19A Nov. 2025 Iraqi Journal of Humanitarian, Social and Scientific Research
Print ISSN 2710-0952 Electronic ISSN 2790-1254

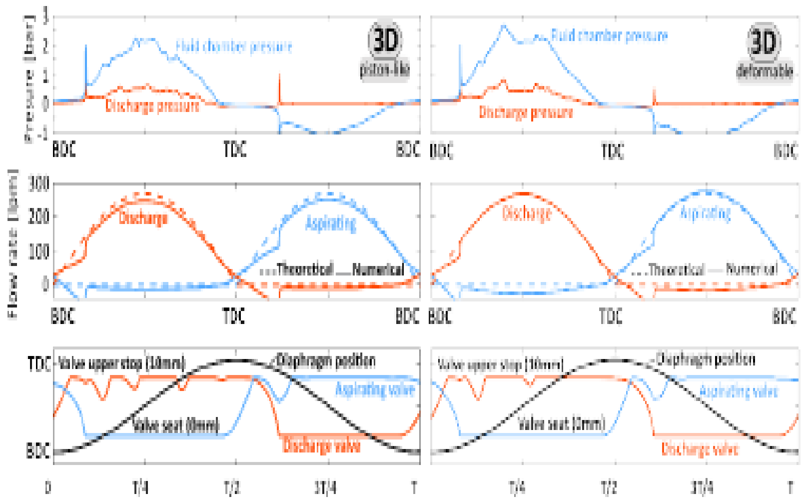


Figure 19. Comparison of temporal evolutions of pressure, flow rate, and check valve responses during the diaphragm cycle between the 3D piston-like model (left) and the 3D deformable diaphragm model (right).

Finally, Figure 20 highlights the differences in flow patterns between the deformable and piston-like diaphragm models, visualized through velocity contours. The left panel shows velocity fields at T/4, corresponding to the peak forward stroke impulse, emphasizing how the diaphragm-driven flow passes through the discharge valve. In the deformable diaphragm model, the flow is more efficiently channeled into the outlet port, forming a well-defined, gradually expanding high-velocity jet around the valve ball. In contrast, the piston-like model exhibits a significant recirculation zone within the rectangular cavity connecting the working chamber to the outlet manifold, which correlates with the higher volumetric losses reported in Figure 19.

The right panel presents velocity maps at 3T/4, during the backward stroke, where only subtle differences between the models are observed. Notably, the deformable diaphragm provides increased volume in the lower chamber, allowing for a more gradual distribution of the suction-induced pressure gradient. This contributes to enhanced aspirating conditions and a reduction in flow leakage through the inlet check valve

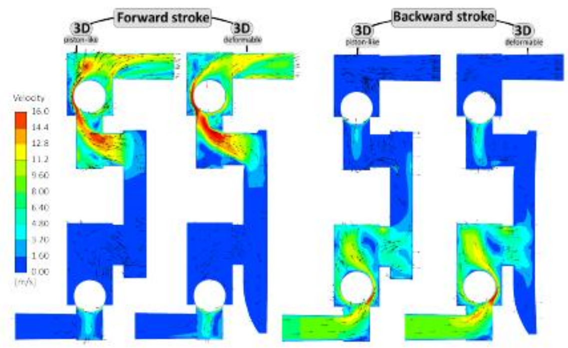


Figure 20. Comparison of flow patterns in the cavities between 3D piston-like model and 3D deformable diaphragm model.

## 5. Conclusions

A comprehensive three-dimensional, unsteady CFD model with dynamic mesh capabilities has been developed and validated to simulate Air-Operated Double Diaphragm (AODD) pumps under various operating conditions. This advanced 3D model builds upon a previously established two-dimensional methodology, enabling a more accurate representation of the complex fluid-structure interactions characteristic of positive displacement pumps.

To enhance computational efficiency, a piston-like diaphragm approximation was initially employed, preserving the volumetric displacement of the real deformable diaphragm while allowing the use of a computationally efficient layering remeshing algorithm. Subsequently, a fully deformable diaphragm model was introduced, confirming that the piston-like approach reliably captures the essential behavior and performance metrics of the system.

Experimental validation showed good agreement with 3D numerical predictions in terms of overall pump performance. Although local pressure measurements within the diaphragm cavity revealed some temporal discrepancies, the time-averaged pressure trends were well represented. Under standard operating conditions, low air-supply pressures (~2 bar) led to increased instabilities and frequent valve tapping, especially in the discharge valve, with up to four partial re-openings observed. Higher supply pressures (6 bar) reduced these oscillations to two re-openings during the forward stroke and improved volumetric efficiency.

Notably, the 2D model tended to excessively damp valve dynamics and fluid-structure interactions, whereas the 3D model more accurately captured rapid inertial effects and valve behavior. Under free-delivery conditions, the 3D simulations predicted more pronounced pressure drops within the diaphragm cavity during suction strokes, with near-vacuum pressures indicating potential cavitation risk and increased volumetric losses consistent with pump efficiency maps.

Finally, valve instabilities were consistently more prominent in the discharge valve compared to the inlet valve, which demonstrated superior sealing and only minor partial re-openings near the backward stroke's start. These insights provide valuable guidance for the design, material selection, and maintenance of critical pump components

**References**

1.Aldi, N., Buratto, C., Pinelli, M., Spina, P.R., Suman, A., Casari, N., 2016. CFD analysis of a non-Newtonian fluids processing pump. Energy Procedia 101, 742–749.

2. Altare, G., Rundo, M., CFD analysis of gerotor lubricating pumps at high speed: Geometric features influencing the filling capability. In: Proceedings of the ASME/BATH 2015 Symposium on Fluid Power and Motion Control, Chicago, IL (USA), October 12–14, 2015.

3.ANSI/HI. 10.1-10.5, 2010. Air Operated Pumps for Nomenclature, Definitions, Application and Operation. Hydraulic Institute. ANSI/HI. 10.6, 2004. Air Operated Pump Tests. Hydraulic Institute. ANSYS-FLUENT Meshing User's Guide. Release 16.2.

4.ANSYS, Inc. 2015. ANSYS-FLUENT User's Guide. Release 16.2. ANSYS, Inc. 2015. Bahrton, S., 2002. Reversing Valve for a Diaphragm Pump. US Patent 6419463 B1.

5.Beune, A., Kuerten, J.G.M., van Heumen, M.P.C., 2012. CFD analysis with fluid-structure interaction of opening high-pressure safety valves. Comput. & Fluids 64, 108–116.

6.Farrell, R., Ezekoye, L.I., Rain, M., Check valve flow and disk lift simulation using CFD. In: Proceedings of ASME Pressure Vessels and Piping Conference, Hawaii (USA), July 16–20, 2017.

7. Frosina, E., Senatore, A., Buono, D., Stelson, K.A., Wang, F., Mohanty, B., Gust, M.J., Vane pump power split transmission: Three dimensional computational fluid dynamic modeling. In: Proceedings of the ASME/BATH 2015 Symposium on Fluid Power and Motion Control, Chicago, IL (USA), October 12–14, 2015.

González-Moratiel, A., 2013. Double-Membrane Central-Flow Pump. EP Patent 2573397 A1.

8. Hwang, I.S., Park, S.J., Oh, W., Lee, Y.L., 2017. Linear compressor discharge valve behavior using a rigid body valve model and a FSI valve model. Int. J. Refrig. 82, 509–519.

9.Iannetti, A., Stickland, M.T., Dempster, W.M., 2014. A computational fluid dynamics model to evaluate the inlet stroke performance of a positive displacement reciprocating plunger pump. Proc. IMechE A 228 (5), 574–584.

10.Iannetti, A., Stickland, M.T., Dempster, W.M., 2015. A CFD study on the mechanisms which cause cavitation in positive displacement reciprocating pumps. J. Hydraul. Eng. 1 (1), 47–59.

11.Iannetti, A., Stickland, M.T., Dempster, W.M., 2016. A CFD and experimental study on cavitation in positive displacement pumps: Benefits and drawbacks of the 'full' cavitation model. Eng. Appl. Comput. Fluid Mech. 10 (1), 57–71.

12. Kumar, S., Bergada, J.M., Watton, J., 2009. Axial piston pump grooved slipper analysis by CFD simulation of three-dimensional NVS equation in cylindrical coordinates. Comput. & Fluids 38, 648–663.

13. Ma, Y., Ni, Y., Zhang, H., Zhou, S., Deng, H., 2018. Influence of valve's lag characteristic on pressure pulsation and performance of reciprocating multiphase pump. J. Petrol. Sci. Eng. 164, 584–594. Menéndez Blanco, A., 2017.

14. Numerical Modelling of Volumetric Diaphragm Pumps (Ph.D. thesis). University of Oviedo, Spain (in Spanish). Menéndez-Blanco, A., Fernández Oro, J.M., 2012. Unsteady numerical simulation of an air-operated piston pump for lubricating greases using dynamic meshes. Comput. & Fluids 57, 138–150.

15.Menéndez-Blanco, A., Fernández Oro, J.M., Meana-Fernández, A., 2019. A numerical methodology for the CFD simulation of diaphragm volumetric pumps. Int. J. Mech. Sci. 150, 322–336.

16.Pan, X., Yang, S., Shi, Y., Liu, Y., 2019. Investigation on the dynamic characteristics of port valves in a diaphragm pump for exhaust gas treatment system by FSI modeling. IEEE Access http://dx.doi.org/10.1109/ACCESS.2019.2914282. Ragoth, R.S., Nataraj, M., 2012. Study on performance of plunger pump at various crank angle using CFD. Eng. Sci. Technol. Int. J. 2 (4), 549–553.

17. van Rijswick, R., Talmon, A., van Rhee, C., 2016. Fluid structure interaction (FSI) in piston diaphragm pumps. Can. J. Chem. Eng. 94 (6), 1116–1126. SAMOA Flow, Online catalogue for Diaphragm Pumps. http://www.samoaindustrial.com/flow/catalogo_directflo_en.html. (Accessed 21 November 2019).

18.Srikanth, C., Bhasker, C., 2009. Flow analysis in valve with moving grids through CFD techniques. Adv. Eng. Softw. 40 (3), 193–201. Tan, Q., Pan, S., Feng, Q., Yu, X., Wang, Z., 2014.

19.Fluid–structure interaction model of dynamic behavior of the discharge valve in a rotary compressor. Proc. IMechE E 229 (4), 280–289.

20.Tao, W., Guo, Y., He, Z., Peng, X., 2018. Investigation on the delayed closure of the suction valve in the refrigerator compressor by FSI modeling. Int. J. Refrig. 91, 111–121.

21.Wang, G., Zhang, L., He, X., Lei, Z., Hu, G., Li, R., Wang, Y., 2015. Dynamic behavior of reciprocating plunger pump discharge valve based on fluid structure interaction and experimental analysis. PLoS One 10 (10), 1–20.

22. Wei, G., 2006. An Implicit Method to Solve Problems of Rigid Body Motion Coupled with Fluid Flow. Technical note, FSI-05-TN76. Flow Science Inc.. Zhang, S.C., Zhang, Y.L., Fang, Z.M., 2012. Numerical simulation and analysis of ball valve three-dimensional flow based on CFD. In: IOP Conference Series: Earth and Environmental Science, vol. 15, 052024